

TECHNICAL
REPORTS:
METHODS

10.1002/2017JA024143

Key Points:

- A 3-D layer method code has been developed and validated
- Radiation belt dynamics is modeled directly using (α_0, p, L) coordinates
- Application to one storm time enhancement event supports acceleration by chorus waves

Supporting Information:

- Supporting Information S1

Correspondence to:

X. Tao,
xtao@ustc.edu.cn

Citation:

Wang, C., et al. (2017), Modeling radiation belt dynamics using a 3-D layer method code, *J. Geophys. Res. Space Physics*, 122, 8642–8658, doi:10.1002/2017JA024143.

Received 14 MAR 2017

Accepted 7 AUG 2017

Accepted article online 14 AUG 2017

Published online 26 AUG 2017

Modeling radiation belt dynamics using a 3-D layer method code

C. Wang^{1,2}, Q. Ma^{3,4}, X. Tao^{1,2}, Y. Zhang⁵, S. Teng^{1,2}, J. M. Albert⁶, A. A. Chan⁷, W. Li⁴, B. Ni⁵, Q. Lu^{1,2}, and S. Wang^{1,2}

¹CAS Key Laboratory of Geospace Environment, Department of Geophysics and Planetary Sciences, University of Science and Technology of China, Hefei, China, ²Collaborative Innovation Center of Astronautical Science and Technology, Hefei, China, ³Department of Atmospheric and Oceanic Sciences, University of California, Los Angeles, California, USA, ⁴Center for Space Physics, Boston University, Boston, Massachusetts, USA, ⁵Department of Space Physics, School of Electronic Information, Wuhan University, Wuhan, China, ⁶Air Force Research Laboratory, Space Vehicles Directorate, Kirtland Air Force Base, Albuquerque, New Mexico, USA, ⁷Department of Physics and Astronomy, Rice University, Houston, Texas, USA

Abstract A new 3-D diffusion code using a recently published layer method has been developed to analyze radiation belt electron dynamics. The code guarantees the positivity of the solution even when mixed diffusion terms are included. Unlike most of the previous codes, our 3-D code is developed directly in equatorial pitch angle (α_0), momentum (p), and L shell coordinates; this eliminates the need to transform back and forth between (α_0, p) coordinates and adiabatic invariant coordinates. Using (α_0, p, L) is also convenient for direct comparison with satellite data. The new code has been validated by various numerical tests, and we apply the 3-D code to model the rapid electron flux enhancement following the geomagnetic storm on 17 March 2013, which is one of the Geospace Environment Modeling Focus Group challenge events. An event-specific global chorus wave model, an AL -dependent statistical plasmaspheric hiss wave model, and a recently published radial diffusion coefficient formula from Time History of Events and Macroscale Interactions during Substorms (THEMIS) statistics are used. The simulation results show good agreement with satellite observations, in general, supporting the scenario that the rapid enhancement of radiation belt electron flux for this event results from an increased level of the seed population by radial diffusion, with subsequent acceleration by chorus waves. Our results prove that the layer method can be readily used to model global radiation belt dynamics in three dimensions.

1. Introduction

The electron flux of the outer radiation belt is highly variable, especially during geomagnetically disturbed times [e.g., *Van Allen and Frank*, 1959; *Meredith et al.*, 2002; *Baker and Kanekal*, 2008], and a complex competition between source and loss processes controls the electron dynamics [e.g., *Summers et al.*, 1998; *Horne and Thorne*, 1998; *Reeves et al.*, 2003; *Tu et al.*, 2009; *Thorne*, 2010; *Turner et al.*, 2014a]. Previous studies proposed that radial diffusion [*Falthammer*, 1965; *Elkington*, 2006; *Ukhorskiy et al.*, 2009; *Li et al.*, 2017], local acceleration driven by wave-particle interactions [*Horne and Thorne*, 1998; *Summers et al.*, 1998; *Reeves et al.*, 2013; *Thorne et al.*, 2013], shock-induced acceleration [e.g., *Li et al.*, 1993, 1997; *Hudson et al.*, 1997], and direct substorm injection [e.g., *Dai et al.*, 2014] might lead to the enhancement of MeV electron fluxes. On the other hand, magnetopause shadowing and wave-driven pitch angle scattering into the loss cone might contribute to the loss of the energetic electrons [e.g., *Thorne and Kennel*, 1971; *Turner et al.*, 2014b; *Shprits et al.*, 2008a]. The relative roles of the various mechanisms in the radiation belt dynamics typically need to be evaluated for each storm.

A common way to model the global dynamics of radiation belt electrons is to use quasi-linear diffusion theory [*Kennel and Engelmann*, 1966; *Lyons*, 1974a, 1974b] and model the evolution of electron phase space density averaged over the gyrophase, the bounce phase, and the drift phase. Several numerical codes to model three-dimensional diffusion processes have been developed [e.g., *Beutier and Boscher*, 1995; *Subbotin and Shprits*, 2009; *Albert et al.*, 2009; *Xiao et al.*, 2010; *Su et al.*, 2010; *Tu et al.*, 2013; *Glauert et al.*, 2014; *Ma et al.*, 2015]. Many of these codes use two sets of coordinates, the equatorial pitch angle (α_0), momentum (p) (or equivalently kinetic energy (E)), and L^* coordinates [*Roederer*, 1970] and the adiabatic invariant coordinates (μ , J , and Φ). The adiabatic invariants are proportional to the actions corresponding to three quasiperiodic motions of particles in the dipole field: gyromotion, bounce motion, and drift motion [*Schulz and Lanzerotti*, 1974].

The local acceleration is performed in (α_0, p) coordinates, and the radial diffusion is modeled at fixed first and second adiabatic invariant coordinates $(\mu$ and J). Because these two sets of coordinates are not aligned in 3-D, numerical interpolation is needed to obtain phase space densities back and forth between these coordinates. The interpolation may lead to artificial numerical diffusion and requires extra computation time; therefore, some studies [e.g., *Subbotin and Shprits*, 2012] have proposed the use of a single grid.

Regardless of which kind of coordinates are used, the traditional implicit and explicit finite difference methods cannot guarantee the positivity of the solution when applied to the diffusion equation with cross diffusion coefficients [Albert, 2004, 2009, 2013]. *Albert and Young* [2005] addressed the numerical problem through diagonalization of the diffusion coefficient matrix by transforming the coordinate system to remove the cross diffusion terms. *Tao et al.* [2008] used a Monte Carlo method, called the Stochastic Differential Equation (SDE) method, to address the negative phase space density (PSD) problem. This method has recently been used to develop a 3-D SDE code by *Zheng et al.* [2014, 2016]. Furthermore, *Tao et al.* [2009] used the layer method proposed by *Milstein and Tretyakov* [2001] to avoid negative PSDs. The layer method is deterministic, even though it is based on the same mathematical theory as the SDE method. The layer method used by *Tao et al.* [2009] requires a large number of grid points to achieve accurate solutions, because a first-order linear interpolation method was used. Recently, *Tao et al.* [2016] proposed the use of the monotone cubic interpolation method with the layer method. The new method, henceforth called the Layer Method with Monotonic Cubic interpolation (LM-MC) method, significantly increases the efficiency by reducing the number of grid points needed. *Tao et al.* [2016] treated a 2-D pitch angle and momentum diffusion problem, and the main purpose of this study is to apply the LM-MC method to the 3-D case.

The remainder of the paper is organized as follows. In section 2 we present the general framework of the layer method and its application to the 3-D quasi-linear diffusion equation written directly in (α_0, p, L) coordinates. In section 3 we illustrate the validity of the new 3-D layer method code by solving a 1-D radial diffusion problem and a 2-D local pitch angle and energy diffusion problem. In section 4 we apply our 3-D layer method to the 17 March 2013 storm time enhancement event. This event is one of the four Geospace Environment Modeling (GEM) challenge events recently selected by the “Quantitative Assessment of Radiation Belt Modeling” (QARBM) focus group. Finally, we summarize our results in section 5.

2. The 3-D LM-MC Code in (α_0, p, L) Coordinates

2.1. A Brief Review of the Layer Method With Monotonic Cubic Interpolation

The diffusive evolution of a quantity f is described by a general d -dimensional diffusion equation

$$\frac{\partial f}{\partial t} = \frac{1}{G} \frac{\partial}{\partial Q_i} \left(G D_{ij} \frac{\partial f}{\partial Q_j} \right), \quad (1)$$

where Q_i is the i th coordinate, t is time, and D_{ij} 's are the diffusion coefficients. The variable G is proportional to the Jacobian factor; e.g., for the radiation belt quasi-linear diffusion equation, the expression of G is given in equation (10) below. The Einstein summation rule is used unless otherwise specified. Indices i and j each vary from 1 to d for a d -dimensional problem. To use the layer method, we first transform the equation to

$$\frac{\partial f}{\partial t} = b_i \frac{\partial f}{\partial Q_i} + \frac{1}{2} a_{ij} \frac{\partial^2 f}{\partial Q_i \partial Q_j} \quad (2)$$

where

$$b_i = \frac{1}{G} \frac{\partial}{\partial Q_j} (G D_{ji}) = \frac{1}{G} \frac{\partial G}{\partial Q_j} D_{ji} + \frac{\partial D_{ji}}{\partial Q_j}, \quad (3)$$

$$a_{ij} = 2D_{ij}. \quad (4)$$

The layer method discretizes the computational space into grid points, like finite difference methods. To obtain the solution of f at time step t_k following the given solution at time step t_{k-1} at the grid point with coordinates $\mathbf{Q} \equiv (Q_1, Q_2, \dots, Q_d)$, one first obtains a $\tilde{\mathbf{Q}}$

$$\tilde{\mathbf{Q}} = \mathbf{Q} + \mathbf{b} \Delta t + \boldsymbol{\sigma} \cdot \Delta \mathbf{W}. \quad (5)$$

Here Δt is the time step, $\mathbf{b} \equiv \{b_i\}$ is a d vector, and the $d \times d$ matrix $\boldsymbol{\sigma}$ is related to $\mathbf{a} \equiv \{a_{ij}\}$ by

$$\boldsymbol{\sigma} \cdot \boldsymbol{\sigma}^T = \mathbf{a}. \quad (6)$$

It is clear that σ is not uniquely defined by equation (6); however, different choices of σ lead to the same solution of f [Tao et al., 2008]. In equation (5), $\Delta \mathbf{W}$ represents one increment of a Wiener random process [Gardiner, 1985], and each component of $\Delta \mathbf{W}$ is a random variable. In layer methods, the probability distribution function (P) of the i th component of $\Delta \mathbf{W}$ is chosen to be $P(\Delta W_i = \pm \sqrt{\Delta t}) = 1/2$ [Milstein, 2002]. Therefore, there are 2^d possible $\tilde{\mathbf{Q}}$ values. The solution at time t_k is then obtained from the previous time step t_{k-1} by

$$f(\mathbf{Q}, t_k) = \frac{1}{2^d} \sum_{i=1}^{2^d} f(\tilde{\mathbf{Q}}_i, t_{k-1}). \quad (7)$$

Note that normally, $\tilde{\mathbf{Q}}_i$ is not located on the grid; therefore, interpolation is required to obtain $f(\tilde{\mathbf{Q}}_i, t_{k-1})$. The layer method is stable for an arbitrary choice of Δt if a monotonicity-preserving interpolation method (e.g., linear interpolation) is used. In practice, we typically choose Δt so that $|\tilde{\mathbf{Q}} - \mathbf{Q}|$ is on the same order as the grid size. For more information about the stability and order of convergence analysis, we refer readers to Milstein [2002], Milstein and Tretyakov [2001], and Milstein and Tretyakov [2002]. Tao et al. [2009] used linear interpolation, for which a large number of grid points is required to obtain accurate results (for a 2-D pitch angle and energy diffusion problem, typically 1000×1000 grid points are needed). Tao et al. [2016] introduced a positivity-preserving and monotonicity-preserving cubic interpolation algorithm, called the ‘‘Carlson-Fritsch-Huynh’’ method [Carlson and Fritsch, 1985; Dougherty et al., 1989; Fritsch and Carlson, 1980; Hyman, 1983; Huynh, 1993]. The resulting layer method, called the LM-MC (Layer Method with Monotonic Cubic interpolation) method, is positivity preserving. The number of grid points used in LM-MC is on the same order as standard finite difference methods. For example, for the 2-D pitch angle and energy diffusion defined in section 3.2, typically, a few tens of grid points for each coordinate are used. Therefore, the LM-MC method is much more efficient than the layer method used by Tao et al. [2009].

2.2. Modeling 3-D Radiation Belt Diffusion in (α_0, p, L) Coordinate Using Layer Method

In this section, we apply the LM-MC method to the 3-D radiation belt diffusion problem. The 3-D quasi-linear equation is written in the three adiabatic invariants space (J_1, J_2, J_3) [e.g., Schulz and Lanzerotti, 1974] as

$$\frac{\partial f}{\partial t} = \frac{\partial}{\partial J_i} \left(D_{J_i J_i} \frac{\partial f}{\partial J_i} \right). \quad (8)$$

We take $J_1 = \mu \equiv p_{\perp}^2 / 2mB$, $J_2 = J = \oint p_{\parallel} ds$, and $J_3 = \Phi$, where m is the mass, B is the magnetic field strength, p_{\perp} and p_{\parallel} are the momentum perpendicular and parallel to the magnetic field, s is the distance along a field line, and Φ is the magnetic flux enclosed by the drift orbit. When written in arbitrary coordinates (Q_1, Q_2, Q_3) , the resulting diffusion equation is

$$\frac{\partial f}{\partial t} = \frac{1}{G} \frac{\partial}{\partial Q_i} \left(G D_{Q_i Q_i} \frac{\partial f}{\partial Q_i} \right), \quad (9)$$

where G is proportional to the transformation Jacobian

$$G \propto \frac{\partial(J_1, J_2, J_3)}{\partial(Q_1, Q_2, Q_3)}. \quad (10)$$

Any constants in G are canceled in equation (9). The diffusion coefficients in Q coordinates are

$$D_{Q_i Q_j} = \frac{\partial Q_i}{\partial J_k} D_{J_k J_l} \frac{\partial Q_j}{\partial J_l}. \quad (11)$$

From now on, we consider a dipole field and write the diffusion equation in (α_0, p, L) coordinates. Here L shell, which is the equatorial crossing distance of a field line in Earth radii, is the same as L^* , which is proportional to $1/\Phi$, for a dipole magnetic field. The adiabatic invariants are related to α_0 , p , and L by

$$\begin{aligned} \mu &= \frac{p^2 \sin^2 \alpha_0}{2m(B_E/L^3)}, \\ J &= 2pLR_E Y(y), \\ \Phi &= \frac{2\pi B_E R_E^2}{L}, \end{aligned} \quad (12)$$

where $y \equiv \sin \alpha_0$ and $Y(y) = 2T(0)(1-y) + [T(0) - T(1)](y \ln y + 2y - 2\sqrt{y})$ for a dipole field with $T(0) \approx 1.3802$ and $T(1) \approx 0.7405$ [Schulz and Lanzerotti, 1974]. Here B_E is the equatorial magnetic field strength on the Earth's surface. The 3-D radiation belt diffusion in the (α_0, p, L) coordinate system is

$$\begin{aligned} \frac{df}{dt} = & \frac{1}{G} \frac{\partial}{\partial \alpha_0} \left[G \left(D_{\alpha_0 \alpha_0} \frac{\partial f}{\partial \alpha_0} + D_{\alpha_0 p} \frac{\partial f}{\partial p} + D_{\alpha_0 L} \frac{\partial f}{\partial L} \right) \right] \\ & + \frac{1}{G} \frac{\partial}{\partial p} \left[G \left(D_{p \alpha_0} \frac{\partial f}{\partial \alpha_0} + D_{pp} \frac{\partial f}{\partial p} + D_{pL} \frac{\partial f}{\partial L} \right) \right] \\ & + \frac{1}{G} \frac{\partial}{\partial L} \left[G \left(D_{L \alpha_0} \frac{\partial f}{\partial \alpha_0} + D_{Lp} \frac{\partial f}{\partial p} + D_{LL} \frac{\partial f}{\partial L} \right) \right], \end{aligned} \quad (13)$$

where G can be calculated from the Jacobian as

$$\begin{aligned} G & \propto \begin{vmatrix} \partial \mu / \partial \alpha_0 & \partial \mu / \partial p & \partial \mu / \partial L \\ \partial J / \partial \alpha_0 & \partial J / \partial p & \partial J / \partial L \\ \partial \Phi / \partial \alpha_0 & \partial \Phi / \partial p & \partial \Phi / \partial L \end{vmatrix} \\ & \propto \begin{vmatrix} 2p^2 L^3 \sin \alpha_0 \cos \alpha_0 & 2pL^3 \sin^2 \alpha_0 & 3p^2 L^2 \sin^2 \alpha_0 \\ pL \partial Y / \partial \alpha_0 & Y(y)L & Y(y)p \\ 0 & 0 & -1/L^2 \end{vmatrix} \\ & \propto p^2 L^2 \sin \alpha_0 \cos \alpha_0 T(y), \end{aligned} \quad (14)$$

where $T(y) = T(0) - [T(0) - T(1)](y + \sqrt{y})/2$. Therefore, we set $G = p^2 L^2 \sin \alpha_0 \cos \alpha_0 T(y)$.

The diffusion coefficients in (α_0, p, L) coordinates are obtained according to equation (11). Note that in the dipole field, $D_{\mu L}$ and D_{JL} are both zero. Therefore, one can derive, for example,

$$D_{\alpha_0 \alpha_0} = \frac{\partial \alpha_0}{\partial \mu} \left(D_{\mu \mu} \frac{\partial \alpha_0}{\partial \mu} + D_{\mu J} \frac{\partial \alpha_0}{\partial J} \right) + \frac{\partial \alpha_0}{\partial J} \left(D_{J \mu} \frac{\partial \alpha_0}{\partial \mu} + D_{JJ} \frac{\partial \alpha_0}{\partial J} \right) + \left(\frac{\partial \alpha_0}{\partial L} \right)^2 D_{LL} \quad (15)$$

The first two terms on the right-hand side are from the local wave-particle interaction and can be combined to give $\bar{D}_{\alpha_0 \alpha_0}$ that can be calculated from codes such as *Albert* [2005], *PADIE* [Glauert and Horne, 2005], or the *UCLA Full Diffusion Code* [Ni et al., 2008, 2011; Shprits and Ni, 2009]. The third term represents the variation of α_0 due to a change in L . Therefore, we may write $D_{\alpha_0 \alpha_0}$ as

$$D_{\alpha_0 \alpha_0} = \bar{D}_{\alpha_0 \alpha_0} + \left(\frac{\partial \alpha_0}{\partial L} \right)^2 D_{LL}. \quad (16)$$

Similarly, we have for other diffusion coefficients

$$D_{\alpha_0 p} = \bar{D}_{\alpha_0 p} + \frac{\partial \alpha_0}{\partial L} \frac{\partial p}{\partial L} D_{LL}, \quad (17)$$

$$D_{pp} = \bar{D}_{pp} + \left(\frac{\partial p}{\partial L} \right)^2 D_{LL}, \quad (18)$$

$$D_{\alpha_0 L} = \frac{\partial \alpha_0}{\partial L} D_{LL}, \quad (19)$$

$$D_{pL} = \frac{\partial p}{\partial L} D_{LL}. \quad (20)$$

Here \bar{D} represents diffusion coefficients from local wave-particle interactions. It is straightforward to derive that for a dipole field,

$$\frac{\partial \alpha_0}{\partial L} = -\frac{Y(y) \tan \alpha_0}{4T(y) L}, \quad (21)$$

$$\frac{\partial p}{\partial L} = -\frac{p}{L} \frac{6T(y) - Y(y)}{4T(y)}. \quad (22)$$

Because $D_{\alpha_0 L}$ and D_{pL} are typically not 0, the diffusion matrix in (α_0, p, L) coordinates is full. This is related to the fact that radial diffusion keeps the first and second invariants constant, but not α_0 and p . As can be seen from section 2.1, the presence of these cross diffusion terms can be easily handled by the layer method.

To solve the radiation belt diffusion equation using the layer method, we first write equation (13) in the form of equation (2), from which we find that

$$b_1 = \frac{1}{G} \left(D_{\alpha_0 \alpha_0} \frac{\partial G}{\partial \alpha_0} + D_{\alpha_0 p} \frac{\partial G}{\partial p} + D_{\alpha_0 L} \frac{\partial G}{\partial L} \right) + \frac{\partial D_{\alpha_0 \alpha_0}}{\partial \alpha_0} + \frac{\partial D_{\alpha_0 p}}{\partial p} + \frac{\partial D_{\alpha_0 L}}{\partial L} \quad (23)$$

$$b_2 = \frac{1}{G} \left(D_{\alpha_0 p} \frac{\partial G}{\partial \alpha_0} + D_{pp} \frac{\partial G}{\partial p} + D_{pL} \frac{\partial G}{\partial L} \right) + \frac{\partial D_{\alpha_0 p}}{\partial \alpha_0} + \frac{\partial D_{pp}}{\partial p} + \frac{\partial D_{pL}}{\partial L} \quad (24)$$

$$b_3 = \frac{1}{G} \left(D_{\alpha_0 L} \frac{\partial G}{\partial \alpha_0} + D_{pL} \frac{\partial G}{\partial p} + D_{LL} \frac{\partial G}{\partial L} \right) + \frac{\partial D_{\alpha_0 L}}{\partial \alpha_0} + \frac{\partial D_{pL}}{\partial p} + \frac{\partial D_{LL}}{\partial L} \quad (25)$$

$$a_{11} = 2D_{\alpha_0 \alpha_0} \quad (26)$$

$$a_{12} = a_{21} = 2D_{\alpha_0 p} \quad (27)$$

$$a_{13} = a_{31} = 2D_{\alpha_0 L} \quad (28)$$

$$a_{22} = 2D_{pp} \quad (29)$$

$$a_{23} = a_{32} = 2D_{pL} \quad (30)$$

$$a_{33} = 2D_{LL} \quad (31)$$

To obtain components of the σ matrix from equation (6), note that because $a_{ij} = a_{ji}$, $\sigma_{ik}\sigma_{jk} = a_{ij}$ and $\sigma_{jk}\sigma_{ik} = a_{ji}$ are exactly the same. Therefore, for a d -dimensional problem, there are d^2 unknowns and $d^2 - d(d-1)/2$ equations, and we are free to set $d(d-1)/2$ components of σ . In 3-D, to simplify the solution of σ_{ij} , we set $\sigma_{12} = \sigma_{13} = \sigma_{23} = 0$; i.e.,

$$\sigma_{ij} = \begin{pmatrix} \sigma_{11} & \sigma_{12} & \sigma_{13} \\ \sigma_{21} & \sigma_{22} & \sigma_{23} \\ \sigma_{31} & \sigma_{32} & \sigma_{33} \end{pmatrix} = \begin{pmatrix} \sigma_{11} & 0 & 0 \\ \sigma_{21} & \sigma_{22} & 0 \\ \sigma_{31} & \sigma_{32} & \sigma_{33} \end{pmatrix} \quad (32)$$

From equations $\sigma_{ik}\sigma_{jk} = a_{ij}$, we have

$$\sigma_{11}^2 = a_{11} \Rightarrow \sigma_{11} = \sqrt{2D_{\alpha_0 \alpha_0}} \quad (33)$$

$$\sigma_{11}\sigma_{21} = a_{12} \Rightarrow \sigma_{21} = 2D_{\alpha_0 p}/\sigma_{11} \quad (34)$$

$$\sigma_{11}\sigma_{31} = a_{13} \Rightarrow \sigma_{31} = 2D_{\alpha_0 L}/\sigma_{11} \quad (35)$$

$$\sigma_{21}^2 + \sigma_{22}^2 = a_{22} \Rightarrow \sigma_{22} = \sqrt{2D_{pp} - \sigma_{21}^2} \quad (36)$$

$$\sigma_{21}\sigma_{31} + \sigma_{22}\sigma_{32} = a_{23} \Rightarrow \sigma_{32} = (2D_{pL} - \sigma_{21}\sigma_{31})/\sigma_{22} \quad (37)$$

$$\sigma_{31}^2 + \sigma_{32}^2 + \sigma_{33}^2 = a_{33} \Rightarrow \sigma_{33} = \sqrt{2D_{LL} - \sigma_{31}^2 - \sigma_{32}^2} \quad (38)$$

These coefficients are then used in the layer method equations (5) and (7) to solve the 3-D diffusion equation (13).

3. Illustration of the Validity of the 3-D LM-MC Code

3.1. A 1-D Radial Diffusion Problem

In this section, we illustrate the validity our 3-D layer method code by solving a 1-D radial diffusion problem

$$\frac{\partial f}{\partial t} = L^2 \frac{\partial}{\partial L} \left(\frac{D_{LL}}{L^2} \frac{\partial f}{\partial L} \right). \quad (39)$$

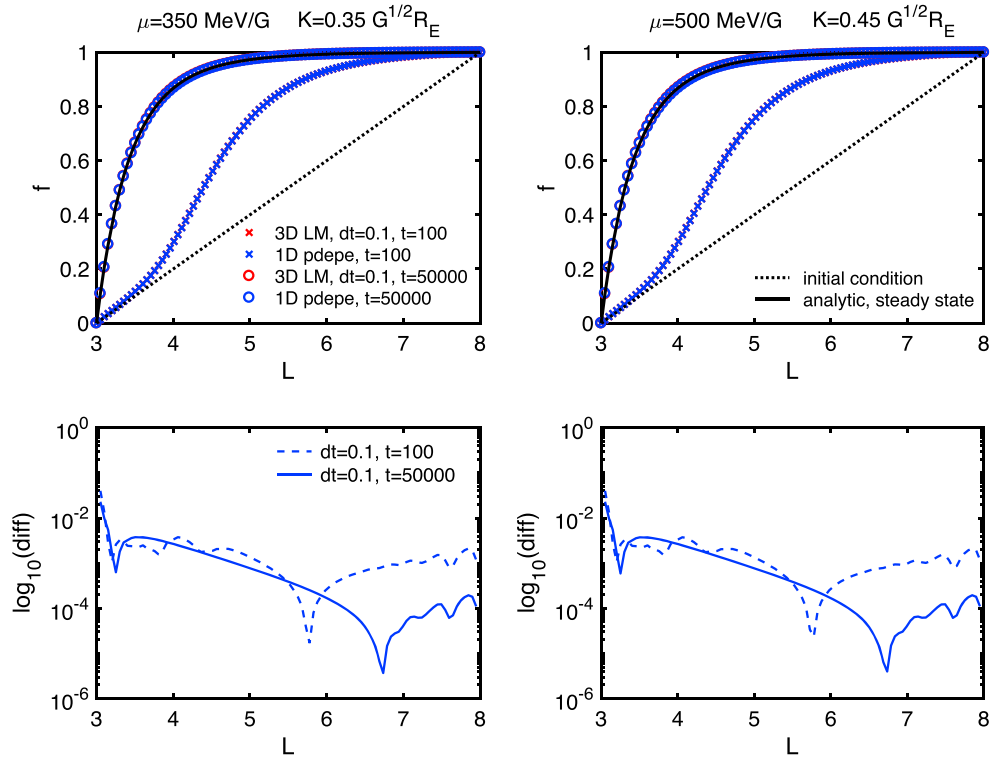


Figure 1. The comparison of the solution of the 1-D diffusion equation at two different (μ, K) 's using different methods. (top row) The black dotted lines and solid lines indicate respectively the initial condition and the steady state solutions of the 1-D diffusion equation; the crosses are the 3-D layer method (LM) results (red) and MATLAB results (blue) at time $t = 100$, and the circles are the 3-D LM solutions (red) and MATLAB solutions (blue) at $t = 50,000$. (bottom row) The relative difference between 3-D LM results and MATLAB results at $t = 100$ (dotted) and $t = 50,000$ (solid).

Here we choose $D_{LL} = L^{10}/10^9$. The factor $1/10^9$ is used so that $D_{LL} \sim 1$ at $L = 8$. The units of D_{LL} and f here are arbitrary. We use fixed boundary conditions so that $f(L = 8) = 1$ and $f(L = 3) = 0$. The analytical steady state solution of this problem is obtained by setting $\partial f / \partial t = 0$, which leads to

$$f_{\text{steady}} = -\frac{3^7 \times 8^7}{8^7 - 3^7} L^{-7} + \frac{8^7}{8^7 - 3^7}. \quad (40)$$

Note that the 1-D radial diffusion equation is derived by assuming a constant μ and J . In this test, we focus on L profiles of the steady state solution of f for two different (μ, K) 's at $(350, 0.35)$ and $(500, 0.45)$ in units of $(\text{MeV}/G, G^{1/2}R_E)$, where K is related to J as $K = J/\sqrt{8m\mu}$. Note that the steady state solution is independent of μ and J since D_{LL} only depends on L .

To solve the problem using our 3-D layer method code in (α_0, p, L) coordinates, we set all local pitch angle and energy diffusion coefficients ($\bar{D}_{\alpha_0\alpha_0}, \bar{D}_{\alpha_0p}$, and \bar{D}_{pp}) to 0. However, none of the components of the diffusion matrix is 0 because of D_{LL} (see equations (16)–(20)). Therefore, the 1-D radial diffusion problem expressed in (α_0, p, L) coordinates is fully 3-D. The simulation domain in α_0 is from 5 to 90° and in E from 0.1 MeV to 10 MeV. The previously selected two (μ, K) 's are located within the simulation domain at all L shells in the 3-D code. The lower and upper boundary conditions in α_0 are $\partial f / \partial \alpha_0 = 0$ for both $\alpha_{0\text{min}}$ and $\alpha_{0\text{max}}$, and in E is $\partial f / \partial p = 0$ for both E_{min} and E_{max} . The initial condition in the simulation is simply chosen to be $f(\alpha_0, p, L) = (L - 3)/5$, satisfying the boundary conditions. The number of grid points used in the 3-D simulation is $N_{\alpha_0} = 40, N_p = 50$, and $N_L = 40$. The time step used is $\Delta t = 0.1$, whose unit is consistent with that of D_{LL} .

The results from our 3-D layer method simulations are compared with the analytical solutions in Figure 1. Also shown in Figure 1 are the solutions obtained by solving the 1-D radial diffusion equation using the pdepe function from MATLAB [MATLAB, 2016] and the relative difference between MATLAB results and the 3-D layer method code results defined by

$$\text{diff} = \frac{|f_M - f_{3D}|}{f_M}, \quad (41)$$

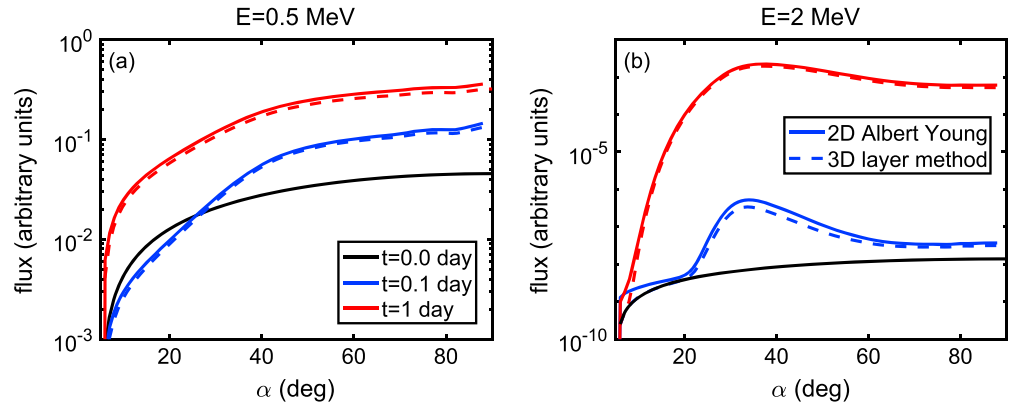


Figure 2. The comparison of flux evolution between the 3-D layer method results (dashed lines) and the solutions using *Albert and Young* [2005] method (solid lines) at time $t = 0.1$ day (blue lines) and $t = 1$ day (red lines) for (a) $E = 0.5$ MeV and (right) $E = 2$ MeV. The black solid lines represent the initial condition.

where f_M is the MATLAB solution and f_{3D} is the 3-D layer method solution. The model results agree well with the analytic solution when the profile reaches the steady state and with the MATLAB solutions at both $t = 100$ and $t = 50,000$. The relative difference is on the order of 10^{-2} at $L = 3$ and 10^{-4} at $L = 8$.

3.2. A 2-D Pitch Angle and Energy Diffusion Problem

The second test we perform here is a local pitch angle and energy diffusion problem presented by *Albert and Young* [2005]. In our 3-D code, we set all $D_{LL} = 0$, and the local pitch angle and momentum diffusion coefficients are chosen to be independent of L and are the same as those used by *Albert and Young* [2005]. The boundary conditions and the initial condition are chosen to be consistent with those of *Albert and Young* [2005], which are

$$f(\alpha_0 = \alpha_{LC}, p, L) = 0, \tag{42}$$

$$\frac{\partial f}{\partial \alpha_0}(\alpha_0 = 90^\circ, p, L) = 0, \tag{43}$$

$$f(\alpha_0, E_{\min} = 0.2 \text{ MeV}, L) = \exp[-(E_{\min} - 0.2)/0.1][\sin(\alpha_0) - \sin(\alpha_{LC})]/p_{\min}^2, \tag{44}$$

$$f(\alpha_0, E_{\max} = 5 \text{ MeV}, L) = 0, \tag{45}$$

where the loss cone angle $\alpha_{LC} = 5^\circ$ at all L 's for simplicity. The initial condition is

$$f(\alpha_0, p, L) = \exp[-(E - 0.2)/0.1][\sin(\alpha_0) - \sin(\alpha_{LC})]/p^2. \tag{46}$$

The number of grid points used is $N_{\alpha_0} = 90$, $N_p = 80$, and $N_L = 40$. The time step is $\Delta t = 5.17$ s.

For this case, our 3-D layer method code results are independent of L . In Figure 2, the electron fluxes $j = p^2 f$ at 0.1 day and 1 day for $E = 0.5$ MeV and $E = 2.0$ MeV are shown. Our 3-D simulation results agree well with the 2-D results from *Albert and Young* [2005]. The relative difference between the two results is about 10^{-1} for both energies at $t = 1$ day near peak fluxes. The small difference is caused by that essentially different equations are solved by *Albert and Young* [2005] and the 3-D LM-MC code, and we refer readers to *Albert and Young* [2005] and *Tao et al.* [2009] for more details. Therefore, both the 1-D and the 2-D validation tests suggest that our 3-D layer method code works as expected. In the next section, we apply the 3-D layer method code to model a storm time enhancement event.

4. Application to the 17 March 2013 Storm

The storm time enhancement event on 17 March 2013 is one of the four selected GEM challenge events. This event has been studied using satellite and ground observations [*Boyd et al.*, 2014; *Foster et al.*, 2014; *Baker et al.*, 2014], with 2-D radiation belt simulations [*Li et al.*, 2014; *Xiao et al.*, 2014] and with a 4-D simulation (with the extra dimension being the magnetic local time) [*Shprits et al.*, 2015]. Previous 2-D simulations have mainly focused on the important roles of electron energization by chorus waves, and the 4-D simulation has analyzed the relative contribution of convective transport and diffusive processes, to the evolution

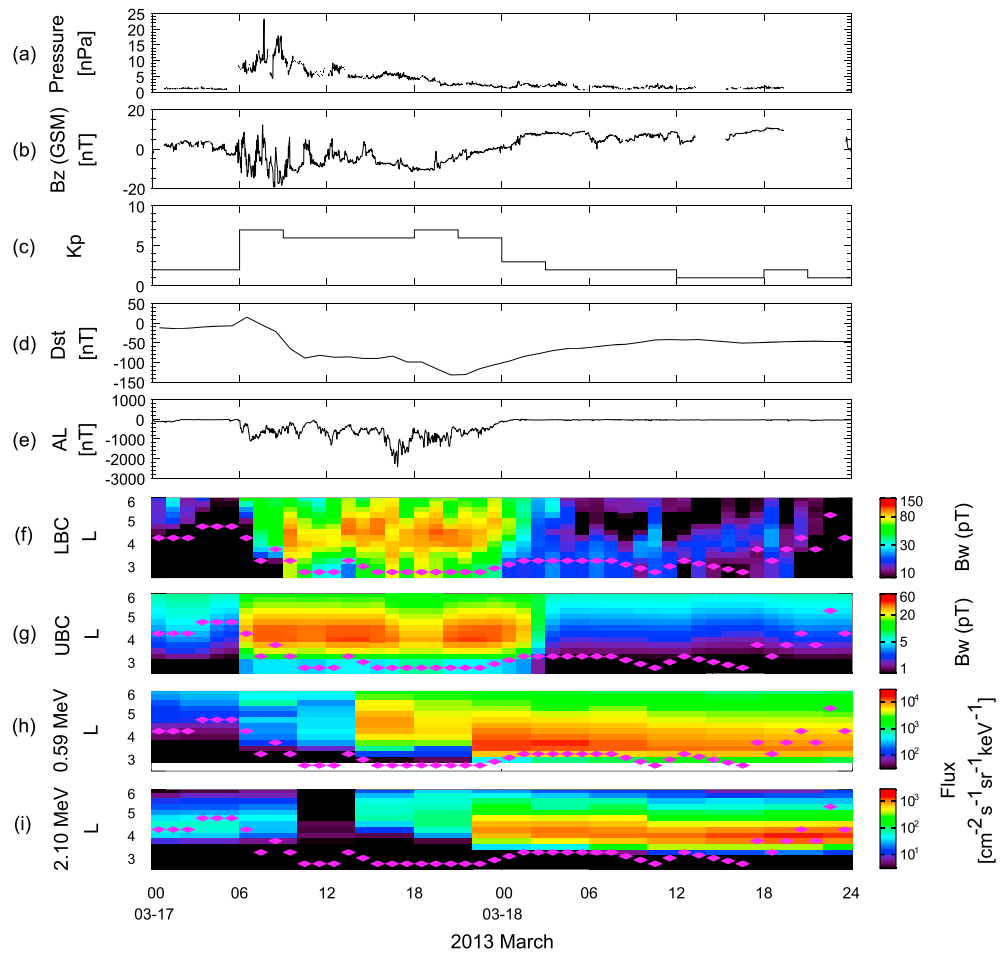


Figure 3. The solar wind parameters, geomagnetic indices, chorus wave amplitudes, and the observed energetic electron fluxes during 17–18 March 2013. (a) Solar wind dynamic pressure, (b) the z component of the interplanetary magnetic field in the GSM coordinates, (c) Kp index, (d) Dst index, (e) AL index, (f) lower band chorus and (g) upper band chorus wave amplitude (B_w) after magnetic local time (MLT) averaging, and (h and i) energetic electron fluxes observed by MagEIS and REPT on both Van Allen Probes A and B at 0.59 MeV and 2.10 MeV, respectively. Purple diamonds show the location of plasmopause in the 04–08 MLT sector determined using Van Allen Probe measurement.

of electron phase space density. Here we perform a 3-D diffusion simulation using the LM-MC code with (α_0, p, L) coordinates to investigate the relative roles of radial diffusion and local wave-particle interaction by chorus waves in the enhancement of outer radiation belt electron flux following this intense geomagnetic storm.

4.1. Overview of the 17 March 2013 Storm

Figure 3 shows an overview of the geomagnetic storm and the response of relativistic electrons during 17–18 March 2013. At 06:04 UT on 17 March 2013, an interplanetary shock reached Earth’s vicinity [Baker et al., 2014] causing a sudden increase of the near-Earth solar wind dynamic pressure (Figure 3a) and dramatic reversals of the z component of interplanetary magnetic field (IMF) (Figure 3b). Accordingly, the Dst index (Figure 3d) rapidly increased up to 15 nT, which represents the sudden commencement of this geomagnetic storm, and then dropped to -90 nT during the storm main phase. The 3 h Kp index (Figure 3c) reached high values close to 7 after 06:00 UT on 17 March, while AL index (Figure 3e) dropped to ~ -1300 nT around 12:00 UT on 17 March. Meanwhile, the relativistic electron fluxes experienced a rapid loss by 1–2 orders at $\sim 12:00$ UT on 17 March (Figure 3i), but hundreds of keV electron fluxes gradually increased (Figures 3h). After 12:00 UT on 17 March, the geomagnetic indices remained at the disturbed levels for several hours and then Dst index and AL index dropped again to ~ -132 nT and ~ -2400 nT, respectively, while the chorus waves intensified and the energetic electron fluxes gradually increased. During the recovery phase from $\sim 21:00$ UT on 17 March,

relativistic electron fluxes exhibited rapid increase and peak flux values are more than 2 orders of magnitude higher than the level of main phase.

This storm is selected as a GEM challenge event to quantitatively assess the relative importance of local acceleration, transport, and loss processes in storm time enhancement events. *Boyd et al.* [2014] presented the phase space density observations and described the electron enhancement process: The seed electrons (typically 30–300 keV electrons [e.g., *Jaynes et al.*, 2015]) were transported to the heart of outer belt, and electrons were subsequently accelerated to multi-MeV energies. *Foster et al.* [2014] reported a substorm occurring at 22:17 UT on 17 March, accompanied by strong chorus waves. *Li et al.* [2014] and *Xiao et al.* [2014] performed 2-D simulations and concluded that the local acceleration driven by chorus waves could produce such significant enhancements of relativistic electrons. *Shprits et al.* [2015] performed a 4-D simulation by including convective transport and analyzed the relative roles of the convective process and other diffusive processes. Although the electron evolution during disturbed periods is controlled by many factors, the relativistic electron enhancement is mostly determined by whistler mode chorus waves and radial diffusion by ULF waves, and the combination of their effects is required to quantitatively explain the observed features. In this paper, we focus on the combined effects of radial transport and local acceleration from 12:00 UT on 17 March to 24:00 UT on 18 March and quantify their relative importance in the observed electron enhancement.

4.2. Model Setup

Assuming a dipole magnetic field, the equation solved by our 3-D LM-MC code is

$$\begin{aligned} \frac{\partial f}{\partial t} = & \frac{1}{G} \frac{\partial}{\partial \alpha_0} \left[G \left(D_{\alpha_0 \alpha_0} \frac{\partial f}{\partial \alpha_0} + D_{\alpha_0 p} \frac{\partial f}{\partial p} + D_{\alpha_0 L} \frac{\partial f}{\partial L} \right) \right] \\ & + \frac{1}{G} \frac{\partial}{\partial p} \left[G \left(D_{p \alpha_0} \frac{\partial f}{\partial \alpha_0} + D_{pp} \frac{\partial f}{\partial p} + D_{pL} \frac{\partial f}{\partial L} \right) \right] \\ & + \frac{1}{G} \frac{\partial}{\partial L} \left[G \left(D_{L \alpha_0} \frac{\partial f}{\partial \alpha_0} + D_{Lp} \frac{\partial f}{\partial p} + D_{LL} \frac{\partial f}{\partial L} \right) \right] - \frac{f}{\tau}. \end{aligned} \quad (47)$$

Compared to equation (13), the term $-f/\tau$ is added to model the precipitation loss to the atmosphere. The parameter τ is set to be a quarter of a bounce period inside the loss cone and infinite outside the loss cone. At a given L , the loss cone is calculated using $\alpha_L = \arcsin[L^5(4L - 3)]^{-1/4}$. We adopt operator splitting [*Strang*, 1968] to handle this loss term.

The evolution of 0.1 MeV to 10 MeV electrons is simulated, from $L = 2.5$ to $L = 6$, which well covers the electron flux enhancement measured by the Van Allen Probes. We use 50 grid points in α_0 , 40 points in energy (E), and 15 points in L shell. The E grid is set as logarithmically evenly spaced. We use $\partial f / \partial \alpha_0 = 0$ at $\alpha_0 = 0$ and 90° as the pitch angle boundary conditions. To infer the phase space densities at the lower and higher L shell and energy boundaries as a function of time, we use Level 3 electron flux data provided by Magnetic Electron Ion Spectrometer (MagEIS) instrument and the Relativistic Electron-Proton Telescope (REPT) instrument [*Baker et al.*, 2013] on board both Van Allen Probes A and B. First, the measured fluxes are converted to phase space densities (PSDs). After mapping into the equatorial pitch angle distributions using TS05 magnetic field model [*Tsyganenko and Sitnov*, 2005], the PSDs are binned into $0.25L \times 4$ h grids at each instrumental energy channels from 12:00 UT on 17 March to 00:00 UT on 19 March. Then, they are interpolated into the (α_0, p) grids we used. To avoid abrupt changes, the boundary conditions are updated every time step by interpolation in time. The initial condition is obtained from measured fluxes within 2 h time window around 12:00 UT on 17 March 2013.

To model the evolution of electron phase space density, we include local wave-particle interactions from chorus and hiss waves and radial diffusion by ULF waves. We refer readers to the supporting information for more details about the diffusion coefficients and wave amplitude distributions.

4.3. Comparison Between Model and Observation

First, we compare the observation with our full simulation results including radial diffusion and local scattering by chorus and hiss waves. Figures 4a and 4b present the comparison between observation and simulation, and Figures 4c and 4d show line plots of the observed and simulated electron (0.59 MeV to 3.4 MeV) flux evolutions at $L = 4.25$, respectively, where the enhancement is most clear. The full simulation result shows acceleration features in reasonable agreement with observation. As described in section 4.1, after 12:00 UT on 17 March, the electron from hundreds of keV to ~ 2 MeV fluxes experienced gradual increase. As noted in *Boyd et al.* [2014], the line plots in Figure 4c indicate that this increase did not happen at the same time

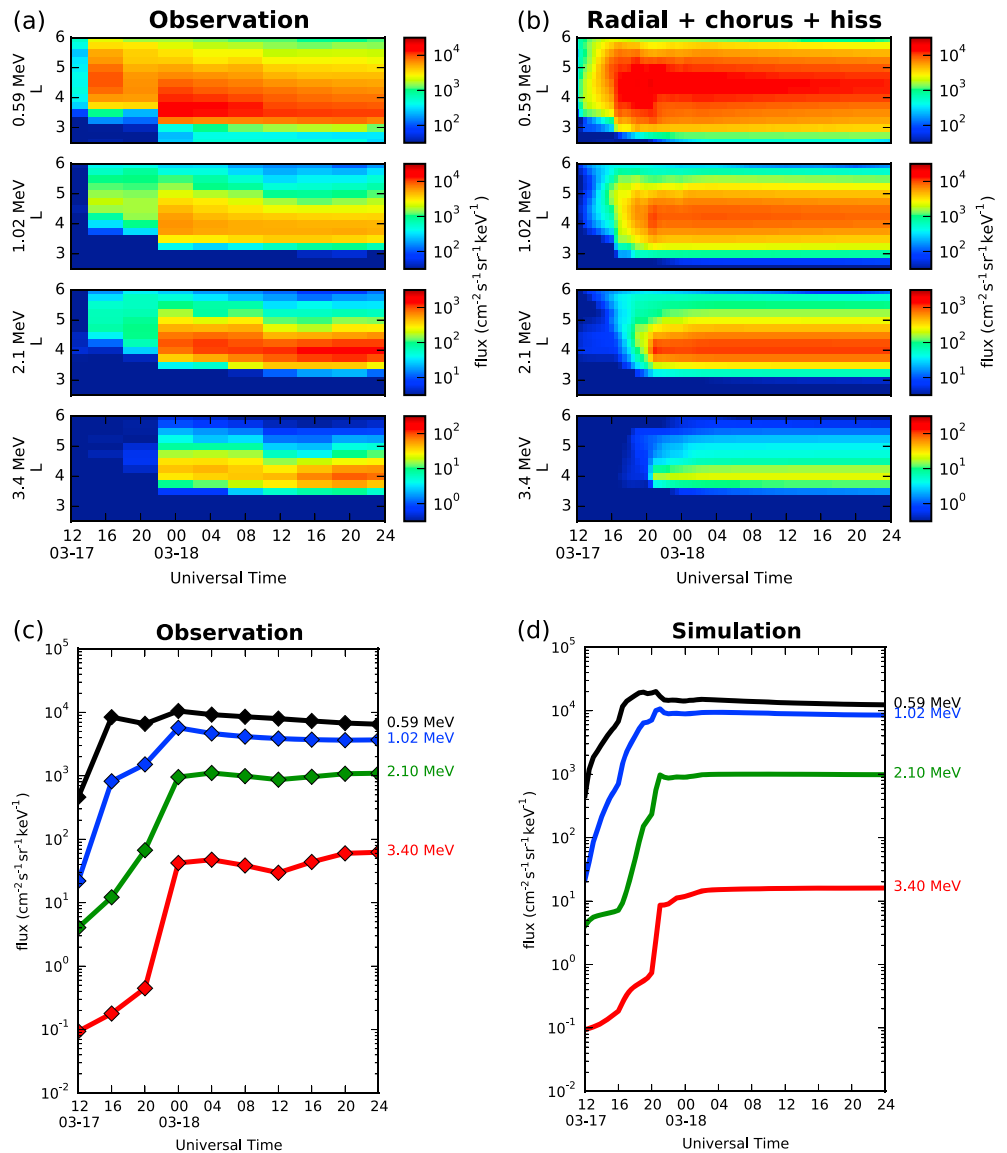


Figure 4. The observed and simulated flux evolution at four different energies. (a) Observed fluxes at 81° pitch angle. (b) Simulation of 81° pitch angle electron evolution by including radial diffusion and local diffusion by chorus and hiss waves. (c) The line plots of observed flux evolutions at $L = 4.25$ and for 81° pitch angle electrons. (d) The line plots of simulated flux evolutions at $L = 4.25$ and for 90° pitch angle electrons. The unit of flux is $(\text{cm}^{-2} \text{s}^{-1} \text{sr}^{-1} \text{keV}^{-1})$.

for all energies. The hundreds of keV electron fluxes rapidly increased from 12:00 UT, followed by the multi-MeV electrons but with a time delay of several hours. The full simulation plots in Figure 4d show similar features: the enhancement of 0.59 MeV electron fluxes starts immediately at 12:00 UT, but the 3.4 MeV electron fluxes begin to increase from around 20:00 UT. The peak location of the simulated 1.02 MeV electron fluxes is located at $L = 4.25$ at 21:00 UT on 17 March, which agrees with the observation ($L \approx 4$). At around 16:00 UT to 20:00 UT on 17 March accompanied with the strongest substorm activities of this event (Figure 3e), the simulated electron fluxes rapidly increased especially at hundreds of keV energies, extending to lower L shells compared with observations. This may be due to the fact that some loss mechanisms are not included in our simulation, such as pitch angle scattering by hiss in plumes [Summers *et al.*, 2008; Li *et al.*, 2014]. At around 24:00 UT on 17 March, the observation fluxes reached the highest level. For example, at $L = 4.25$, the observed 2.1 MeV electron flux at 24:00 UT was a factor of 14 times larger than the flux at 20:00 UT and remained at this high level on 18 March. The full simulation reproduces this feature but in shorter time scale. The simulated increase of 2.1 MeV electron flux is from 20:00 UT and only lasts for about 1 h. The reason

for this “too fast” increase before 21:00 UT is related to the chorus wave activities in our model, which reached the highest level at around 20:00 UT and then gradually decreased (see Figures 3f and 3g). On 18 March, the observed electron fluxes remained at the high level and gradually diffused to lower L shells. The L shell of peak fluxes moved inward by 0.25. But after 06:00 UT on 18 March, the Kp index kept below 2, which makes the radial diffusion in our simulation very weak (the radial diffusion coefficients decrease by a factor of 25 from $Kp = 7$ to $Kp = 2$). So the inward diffusion that occurred on 18 March is not significant, and the 3.4 MeV electron flux is underestimated by the simulation. For example, at 24:00 UT on 18 March, the simulated peak flux of 3.4 MeV electrons at $L = 4$ is a factor of 4 times smaller than the observation. Note that the satellite data are binned at different L shells and UT with a time step of 4 h, while the simulation could resolve the variations with higher time resolution.

Second, we investigate the relative roles of radial diffusion and whistler mode wave scattering in Figure 5 by performing simulations including (1) only radial diffusion (Figure 5a), (2) only pitch angle and energy diffusion by chorus waves (Figure 5b), and (3) both radial diffusion and local scattering by chorus waves (Figure 5c). The full simulation result including all three physical processes is again included (Figure 5d) for comparison. The simulation results that include only radial diffusion based on the formula by *Liu et al.* [2016] show increases in most of the energy channels. However, the magnitude of the flux enhancement is lower than the observation, and the simulated peaks of electron fluxes gradually move inward from the outer boundary ($L = 6$), which is inconsistent with the observation. For example, at 00:00 UT on 18 March, the observed 2.1 MeV electron flux peaks at $L = 4.25$, while the simulated flux peaks at $L = 5.5$, and the simulated peak flux is a factor of 12 times smaller than the observation. By including chorus-driven local acceleration only (Figure 5b), the location and magnitude of the flux enhancement at several hundred keV and ~ 1 MeV energies are roughly consistent with the observation, but the simulated fluxes reach their peak level at around 21:00 UT on 17 March, earlier than the observation as mentioned above. While the simulation may produce the basic shapes of the enhanced flux evolutions at multi-MeV energy channels, the peak magnitudes of the fluxes are weaker than the observation (for example, by a factor of 4 for 3.4 MeV electrons at $L = 4$ at 00:00 UT on 18 March). Simulations adding chorus-driven acceleration to radial diffusion (Figure 5c) cause further acceleration in our model; since chorus is accelerating the seed population to MeV energies, radial diffusion is transporting these inward, providing some additional acceleration. As a consequence, the peak magnitudes of the fluxes in Figure 5c are larger compared with the chorus only results in Figure 5b and are closer to the observation. But the inward radial diffusion also transports several hundred keV electrons from the outer boundary, which leads to the overestimation of 0.59 MeV electron fluxes from around 18:00 UT to 21:00 UT on 18 March. Furthermore, for the observed ~ 3.4 MeV electrons, a secondary enhancement occurred starting from ~ 14 UT on 18 March. Since the chorus waves become weak and Kp reduces after 06 UT on 16 March [*Li et al.*, 2014], our simulation cannot reproduce the further acceleration from 14 UT on 18 March, and the 3.4 MeV electron flux enhancement is underestimated at 24 UT on 18 March. Adding hiss waves to the simulation (Figure 5d) causes slight decrease of electron fluxes especially at lower L shells ($L < 4$) but does not change the overall profile of fluxes mostly outside the plasmopause, suggesting that plasmaspheric hiss waves play a minor role probably due to their limited coverage, but hiss waves in the plume may cause electron flux decrease at high L shells which are not included in our current simulation.

Finally, to investigate the detailed electron flux profiles, we plot the pitch angle distributions of the 0.59 to 3.40 MeV electron fluxes at the final time of the simulation and at four selected L shells of 3.75, 4.25, 4.75, and 5.25. We compared observations (black solid lines in Figure 6) with different simulation results: including only radial diffusion (referred to as “radial only”), including local scattering by chorus waves (referred to as “chorus only”), including both radial diffusion and local scattering by chorus waves (referred to as “radial + chorus”), and including both radial diffusion and local scattering by chorus and hiss waves (referred to as “full”). Although the results of the radial-only simulation are close to the observation at high L shells (for example, at $L = 5.25$ for 1.02 MeV and 2.1 MeV electron fluxes), the simulation results are lower than observation by a few orders of magnitude at MeV energies in the core region of the outer belt ($L \sim 4.25$), which is consistent with previous conclusions [*Brautigam and Albert*, 2000; *Li et al.*, 2009; *Xiao et al.*, 2014], and demonstrates again that the radial diffusion-only model cannot account for the local acceleration at $L \sim 4.25$ observed by the Van Allen Probes. We also note that in the 0.59 MeV energy channel, the radial diffusion results obviously underestimate the flux at $L = 3.75$, roughly match observation at $L = 4.25$, and overestimate the flux at $L = 4.75$ and 5.25. This discrepancy may be caused by the inefficient radial diffusion in our simulation after ~ 06 UT on 18 March when Kp was less than ~ 2 , while the observed electron fluxes

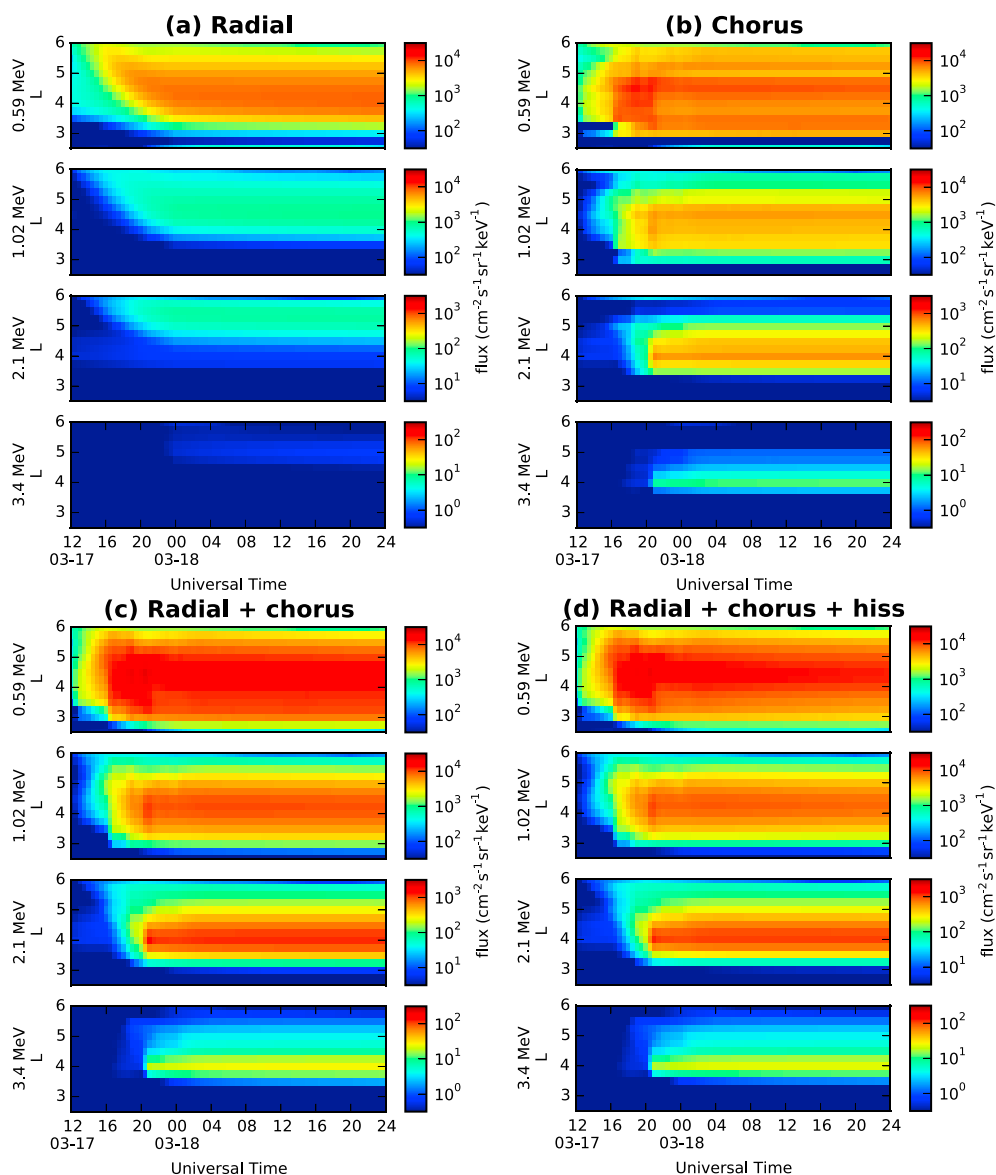


Figure 5. The comparison of simulated flux evolutions using different diffusion models: (a) simulation results by including radial diffusion only, (b) by only including local diffusion by chorus waves, (c) by including both radial diffusion and local diffusion by chorus waves, and (d) by including radial diffusion and local diffusion by chorus and hiss waves. The unit of flux is $(\text{cm}^{-2}\text{s}^{-1}\text{sr}^{-1}\text{keV}^{-1})$. The simulation results are presented at 81° pitch angle.

decreased near the higher L shell boundary. By including only chorus waves, the simulated pitch angle distributions at $E = 2.10$ MeV are roughly consistent with the observation especially at large pitch angles. The formation of the “flat-top” pitch angle distribution, which is the result of local scattering by chorus waves, matches well with previous studies by *Li et al.* [2014] and *Horne et al.* [2003]. However, the chorus-only simulation generally underestimates the peak flux values of several MeV electrons, which indicates that the fluxes of multi-MeV electrons could not be accelerated to the observed level only by chorus. Compared with the results of chorus-only model and radial diffusion-only model, the simulation including radial diffusion and local scattering by chorus shows the joint effort of these two important acceleration mechanisms, especially at multi-MeV energies. Finally, when the effects of radial diffusion, chorus, and hiss waves are all included, the full simulation gives the closest results to the observational profiles in most of the cases. Pitch angle scattering due to plasmaspheric hiss slightly reduces the electron fluxes, which is most evident at lower L shells and at several hundreds of keV energies and consistent with previous studies [*Meredith et al.*, 2006, 2007; *Shprits et al.*, 2008b; *Ni et al.*, 2014; *Ma et al.*, 2016]. The observed electron pitch angle profiles are energy

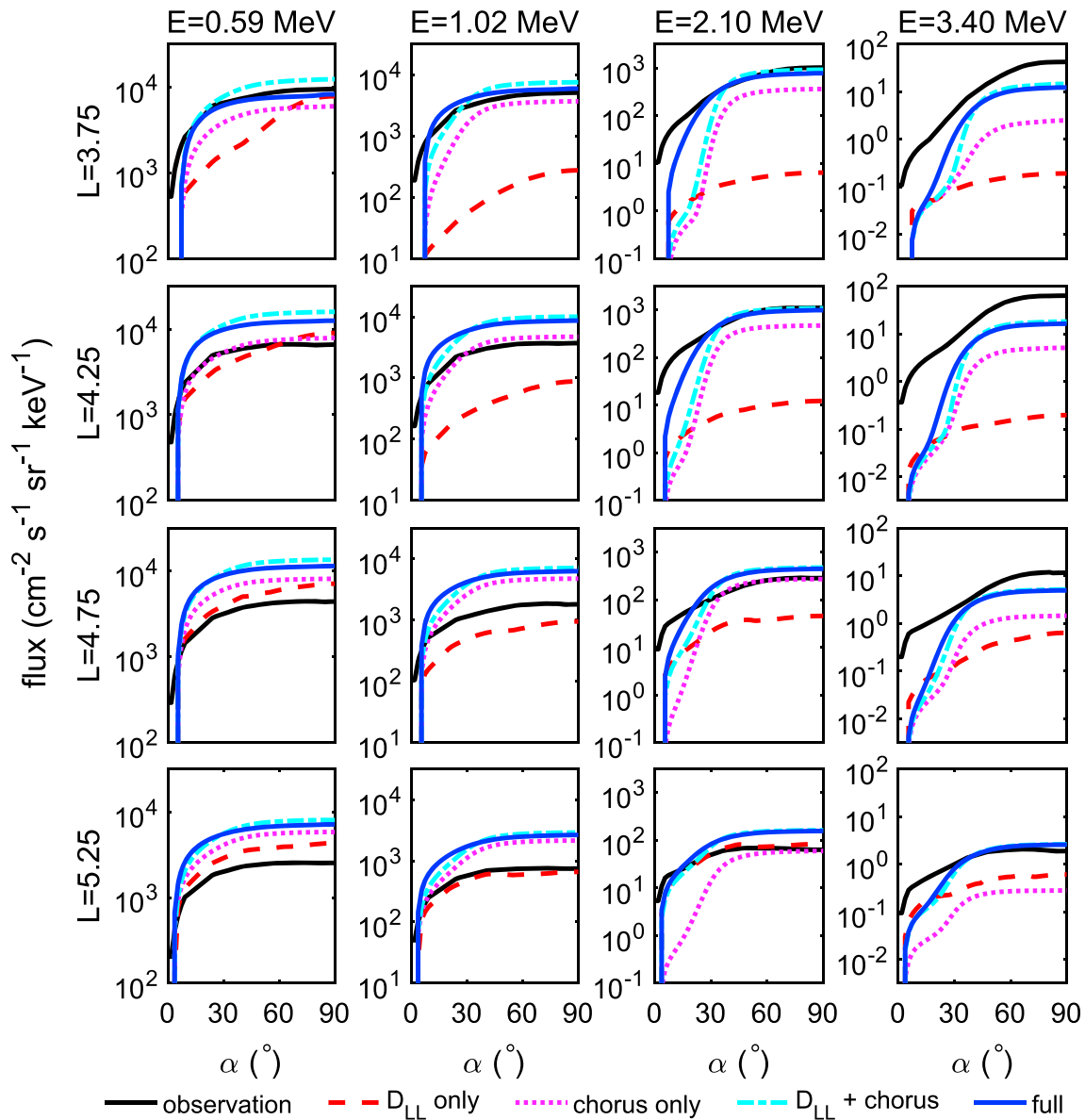


Figure 6. Pitch angle distributions of electron fluxes for energies of 0.59, 1.02, 2.10, and 3.40 MeV and four different L shells at 24:00 UT on 18 March. The black solid lines represent the observational results. Different lines indicate different simulation cases, including radial diffusion only (red dashed lines), local acceleration due to chorus waves only (magenta dotted lines), both radial diffusion and local acceleration due to chorus waves (cyan dash-dotted lines), and both radial diffusion and local diffusion due to chorus and hiss waves (solid blue lines).

dependent. At lower energies (0.59 and 1.02 MeV), the pitch angle distributions are more flattened, while there are larger gradients toward the loss cone at multi-MeV energies (2.10 and 3.40 MeV). The energy-dependent anisotropy is reasonably reproduced in our simulations, which is a consequence of energy-dependent pitch angle scattering and energization.

5. Conclusions

In this study, we developed a 3-D diffusion code using the LM-MC method recently proposed by *Tao et al.* [2016]. This method combines the Milstein-Tretyakov layer method with a positivity- and monotonicity-preserving interpolation method, and the resulting algorithm preserves positive results. We presented the three-dimensional radiation belt diffusion equation directly in (α_0, p, L) coordinates, removing the transformation between adiabatic invariant coordinates and (α_0, p) coordinates. As far as we are aware, this is the first 3-D diffusion code directly using only the (α_0, p, L) coordinate system. The layer method can easily

incorporate the full matrix of 3-D diffusion coefficients, allowing it to handle more complicated physical processes. The use of (α_0, p, L) coordinates also allows a more direct comparison with observations. Our 3-D LM-MC code is validated by solving a 1-D radial diffusion problem and a 2-D local pitch angle and energy diffusion problem. We conclude from these validation tests that the 3-D LM-MC codes can be used in modeling the flux evolutions in the radiation belt.

We apply the 3-D LM-MC code to modeling the rapid electron flux enhancement following the geomagnetic storm on 17 March 2013, which is a challenge event chosen by the GEM radiation belt community. We used the event-specific chorus wave models and diffusion coefficients provided by the GEM QARBM focus group, the latest statistical plasmaspheric hiss wave model, and an energy-dependent radial diffusion model. The simulation reasonably reproduces the essential features of the 17 March event, including the significant enhancement of relativistic electrons in a short time scale, the timing and location of the most significant electron flux enhancement, and the energy-dependent pitch angle distribution profiles. Our results suggest that the seed electron population transported by radial diffusion and the further robust local acceleration driven by chorus waves are the most important factors for this storm time enhancement, which supports previous 2-D simulation results [Li *et al.*, 2014; Xiao *et al.*, 2014]. The joint chorus wave acceleration and radial diffusion causes the most evident flux enhancements for multi-MeV electrons. Our study proves that the proposed LM-MC method is fully applicable to modeling various electron features in the Earth's outer radiation belt.

Finally, we discuss some limitations of our study. For the model, the boundary condition at $\alpha_0 = 90^\circ$ could be extended to the zero-flux-crossing boundary condition by Zheng *et al.* [2014] and Albert *et al.* [2016]. For the GEM challenge event, our simulation did not resolve the flux decay at $L \approx 6$ and the inward diffusion of 3.4 MeV electrons near their peak location after 14:00 UT on 18 March, because the Kp -dependent radial diffusion coefficients are very low in this period. A more accurate event-specific radial diffusion model, instead of the current formula based on instantaneous Kp index, may improve the simulation results on 18 March. As mentioned in Liu *et al.* [2016], the analytic radial diffusion coefficients should be used with care for $\mu < 400$ MeV/G electrons, which corresponds to $E < 1$ MeV at $L = 4$ or $E < 0.41$ MeV at $L = 6$ for the 90° pitch angle electrons. This may explain the overestimation of 0.59 MeV electron fluxes at around 21:00 UT on 17 March. During this period, the strong radial diffusion moves several hundred keV electrons inward in the simulation, leading to the rapid enhancement of energetic electron fluxes and the overestimate compared to the observation. Also, from 18:00 UT to 22:00 UT on 17 March, the slight decrease of the observed energetic electron fluxes indicates that some potential loss mechanisms such as magnetopause shadowing or pitch angle scattering by hiss waves in the plasmaspheric plume should be investigated. The potential effects of event-specific hiss model and other wave modes including electromagnetic ion cyclotron waves [Lyons *et al.*, 1972; Li *et al.*, 2007; Kersten *et al.*, 2014] and magnetosonic waves [Horne *et al.*, 2007; Albert *et al.*, 2016; Li *et al.*, 2016] may also improve our modeling results. These effects will be investigated in future applications of our 3-D layer method code.

Acknowledgments

We acknowledge support by National Natural Science Foundation of China (grants 41474142, 41631071, 41421063, 41204120, 41474141, and 41674163). W. Li at Boston University would like to acknowledge the AFOSR grant FA9550-15-1-0158 and the NSF grant AGS-1723588. The simulation data for this paper are available by contacting the corresponding author. The Van Allen Probes data are obtained from https://rbsp-ect.lanl.gov/data_pub/. We acknowledge the "Quantitative Assessment of Radiation Belt Modeling" GEM focus group for providing the wave amplitudes and diffusion coefficients for this study (http://aten.igpp.ucla.edu/gemwiki/index.php/FG:_Quantitative_Assessment_of_Radiation_Belt_Modeling#RB_dropout_and_'RB_buildup'_Challenge:_Shared_Resources). We also thank CDAWeb for providing the solar wind pressure, IMF B_z , Kp , Dst , and AL data.

References

- Albert, J. M. (2004), Using quasi-linear diffusion to model acceleration and loss from wave-particle interactions, *Space Weather*, 2, S09S03, doi:10.1029/2004SW000069.
- Albert, J. M. (2005), Evaluation of quasi-linear diffusion coefficients for whistler mode waves in a plasma with arbitrary density ratio, *J. Geophys. Res.*, 110, A03218, doi:10.1029/2004JA010844.
- Albert, J. M. (2009), The coupling of quasi-linear pitch angle and energy diffusion, *J. Atmos. Sol. Terr. Phys.*, 71, 1664–1668, doi:10.1016/j.jastp.2008.11.014.
- Albert, J. M. (2013), Comment on "On the numerical simulation of particle dynamics in the radiation belt. Part I: Implicit and semi-implicit schemes" and "On the numerical simulation of particle dynamics in the radiation belt. Part II: Procedure based on the diagonalization of the diffusion tensor" by E. Camporeale et al., *J. Geophys. Res. Space Physics*, 118, 7762–7764, doi:10.1002/2013JA019126.
- Albert, J. M., and S. L. Young (2005), Multidimensional quasi-linear diffusion of radiation belt electrons, *Geophys. Res. Lett.*, 32, L14110, doi:10.1029/2005GL023191.
- Albert, J. M., N. P. Meredith, and R. B. Horne (2009), Three-dimensional diffusion simulation of outer radiation belt electrons during the 9 October 1990 magnetic storm, *J. Geophys. Res.*, 114, A09214, doi:10.1029/2009JA014336.
- Albert, J. M., M. J. Starks, R. B. Horne, N. P. Meredith, and S. A. Glauert (2016), Quasi-linear simulations of inner radiation belt electron pitch angle and energy distributions, *Geophys. Res. Lett.*, 43, 2381–2388, doi:10.1002/2016GL067938.
- Baker, D., and S. Kanekal (2008), Solar cycle changes, geomagnetic variations, and energetic particle properties in the inner magnetosphere, *J. Atmos. Sol. Terr. Phys.*, 70(2), 195–206, doi:10.1016/j.jastp.2007.08.031.
- Baker, D., et al. (2013), The Relativistic Electron-Proton Telescope (REPT) instrument on board the Radiation Belt Storm Probes (RBSP) spacecraft: Characterization of Earth's radiation belt high-energy particle populations, *Space Sci. Rev.*, 179(1–4), 337–381, doi:10.1007/s11214-012-9950-9.
- Baker, D. N., et al. (2014), Gradual diffusion and punctuated phase space density enhancements of highly relativistic electrons: Van Allen Probes observations, *Geophys. Res. Lett.*, 41, 1351–1358, doi:10.1002/2013GL058942.

- Beutier, T., and D. Boscher (1995), A three-dimensional analysis of the electron radiation belt by the Salammbô code, *J. Geophys. Res.*, *100*(A8), 14,853–14,861, doi:10.1029/94JA03066.
- Boyd, A. J., H. E. Spence, S. Claudepierre, J. F. Fennell, J. Blake, D. Baker, G. Reeves, and D. Turner (2014), Quantifying the radiation belt seed population in the 17 March 2013 electron acceleration event, *Geophys. Res. Lett.*, *41*, 2275–2281, doi:10.1002/2014GL059626.
- Brautigam, D. H., and J. M. Albert (2000), Radial diffusion analysis of outer radiation belt electrons during the October 9, 1990, magnetic storm, *J. Geophys. Res.*, *105*(A1), 291–309, doi:10.1029/1999JA900344.
- Carlson, R. E., and F. N. Fritsch (1985), Monotone piecewise bicubic interpolation, *SIAM J. Numer. Anal.*, *22*(2), 386–400, doi:10.1137/0722023.
- Dai, L., J. R. Wygant, C. A. Cattell, S. Thaller, K. Kersten, A. Breneman, X. Tang, R. H. Friedel, S. G. Claudepierre, and X. Tao (2014), Evidence for injection of relativistic electrons into the Earth's outer radiation belt via intense substorm electric fields, *Geophys. Res. Lett.*, *41*, 1133–1141, doi:10.1002/2014GL059228.
- Dougherty, R. L., A. S. Edelman, and J. M. Hyman (1989), Nonnegativity-, monotonicity-, or convexity-preserving cubic and quintic Hermite interpolation, *Math. Comput.*, *52*(186), 471–494, doi:10.1090/S0025-5718-1989-0962209-1.
- Elkington, S. R. (2006), A review of ULF interactions with radiation belt electrons, in *Magnetospheric ULF Waves: Synthesis and new Directions*, pp. 177–193, AGU, Washington, D. C., doi:10.1029/169GM12.
- Falthammar, C. G. (1965), Effects of time-dependent electric fields on geomagnetically trapped radiation, *J. Geophys. Res.*, *70*, 2503–2516, doi:10.1029/JZ070i011p02503.
- Foster, J. C., et al. (2014), Prompt energization of relativistic and highly relativistic electrons during a substorm interval: Van Allen Probes observations, *Geophys. Res. Lett.*, *41*, 20–25, doi:10.1002/2013GL058438.
- Fritsch, F., and R. Carlson (1980), Monotone piecewise cubic interpolation, *SIAM J. Numer. Anal.*, *17*(2), 238–246, doi:10.1137/0717021.
- Gardiner, C. W. (1985), *Handbook of Stochastic Methods for Physics, Chemistry and the Natural Sciences*, Springer, Berlin.
- Glauert, S. A., and R. B. Horne (2005), Calculation of pitch angle and energy diffusion coefficients with the PADIE code, *J. Geophys. Res.*, *110*, A04206, doi:10.1029/2004JA010851.
- Glauert, S. A., R. B. Horne, and N. P. Meredith (2014), Three-dimensional electron radiation belt simulations using the BAS Radiation Belt Model with new diffusion models for chorus, plasmaspheric hiss, and lightning-generated whistlers, *J. Geophys. Res. Space Physics*, *119*, 268–289, doi:10.1002/2013JA019281.
- Horne, R. B., and R. M. Thorne (1998), Potential waves for relativistic electron scattering and stochastic acceleration during magnetic storms, *Geophys. Res. Lett.*, *25*(15), 3011–3014, doi:10.1029/98GL01002.
- Horne, R. B., N. P. Meredith, R. M. Thorne, D. Heynderickx, R. H. A. Iles, and R. R. Anderson (2003), Evolution of energetic electron pitch angle distributions during storm time electron acceleration to megaelectronvolt energies, *J. Geophys. Res.*, *108*, A11016, doi:10.1029/2001JA009165.
- Horne, R. B., R. M. Thorne, S. A. Glauert, N. P. Meredith, D. Pokhotelov, and O. Santolik (2007), Electron acceleration in the Van Allen radiation belts by fast magnetosonic waves, *Geophys. Res. Lett.*, *34*, L17107, doi:10.1029/2007GL030267.
- Hudson, M., S. Elkington, J. Lyon, V. Marchenko, I. Roth, M. Temerin, J. Blake, M. Gussenhoven, and J. Wygant (1997), Simulations of radiation belt formation during storm sudden commencements, *J. Geophys. Res.*, *102*(A7), 14,087–14,102, doi:10.1029/97JA03995.
- Huynh, H. T. (1993), Accurate monotone cubic interpolation, *SIAM J. Numer. Anal.*, *30*(1), 57–100, doi:10.1137/0730004.
- Hyman, J. M. (1983), Accurate monotonicity preserving cubic interpolation, *SIAM J. Sci. Stat. Comput.*, *4*(4), 645–654, doi:10.1137/0904045.
- Jaynes, A. N., et al. (2015), Source and seed populations for relativistic electrons: Their roles in radiation belt changes, *J. Geophys. Res. Space Physics*, *120*, 7240–7254, doi:10.1002/2015JA021234.
- Kennel, C. F., and F. Engelmann (1966), Velocity space diffusion from weak plasma turbulence in a magnetic field, *Phys. Fluids*, *9*(12), 2377–2388, doi:10.1063/1.1761629.
- Kersten, T., R. B. Horne, S. A. Glauert, N. P. Meredith, B. J. Fraser, and R. S. Grew (2014), Electron losses from the radiation belts caused by EMIC waves, *J. Geophys. Res. Space Physics*, *119*, 8820–8837, doi:10.1002/2014JA020366.
- Li, J., et al. (2016), Formation of energetic electron butterfly distributions by magnetosonic waves via Landau resonance, *Geophys. Res. Lett.*, *43*, 3009–3016, doi:10.1002/2016GL067853.
- Li, W., Y. Y. Shprits, and R. M. Thorne (2007), Dynamic evolution of energetic outer zone electrons due to wave-particle interactions during storms, *J. Geophys. Res.*, *112*, A10220, doi:10.1029/2007JA012368.
- Li, W., et al. (2014), Radiation belt electron acceleration by chorus waves during the 17 March 2013 storm, *J. Geophys. Res. Space Physics*, *119*, 4681–4693, doi:10.1002/2014JA019945.
- Li, X., I. Roth, M. Temerin, J. R. Wygant, M. K. Hudson, and J. B. Blake (1993), Simulation of the prompt energization and transport of radiation belt particles during the March 24, 1991 SSC, *Geophys. Res. Lett.*, *20*(22), 2423–2426, doi:10.1029/93GL02701.
- Li, X., D. Baker, M. Temerin, D. Larson, R. Lin, G. Reeves, M. Looper, S. Kanekal, and R. Mewaldt (1997), Are energetic electrons in the solar wind the source of the outer radiation belt?, *Geophys. Res. Lett.*, *24*(8), 923–926, doi:10.1029/97GL00543.
- Li, X., A. B. Barker, D. Baker, W. Tu, T. Sarris, R. Selesnick, R. Friedel, and C. Shen (2009), Modeling the deep penetration of outer belt electrons during the “Halloween” magnetic storm in 2003, *Space Weather*, *7*(2), S02004, doi:10.1029/2008SW000418.
- Li, Z., M. Hudson, M. Patel, M. Wiltberger, A. Boyd, and D. Turner (2017), ULF wave analysis and radial diffusion calculation using a global MHD model for the 17 March 2013 and 2015 storms, *J. Geophys. Res. Space Physics*, *122*, 7353–7363, doi:10.1002/2016JA023846.
- Liu, W., W. Tu, X. Li, T. Sarris, Y. Khotyaintsev, H. Fu, H. Zhang, and Q. Shi (2016), On the calculation of electric diffusion coefficient of radiation belt electrons with in situ electric field measurements by THEMIS, *Geophys. Res. Lett.*, *43*, 1023–1030, doi:10.1002/2015GL067398.
- Lyons, L. R. (1974a), General relations for resonant particle diffusion in pitch angle and energy, *J. Plasma Phys.*, *12*, 45–49, doi:10.1017/S0022377800024910.
- Lyons, L. R. (1974b), Pitch angle and energy diffusion coefficients from resonant interactions with ion-cyclotron and whistler waves, *J. Plasma Phys.*, *12*, 417–432, doi:10.1017/S002237780002537X.
- Lyons, L. R., R. M. Thorne, and C. F. Kennel (1972), Pitch-angle diffusion of radiation belt electrons within the plasmasphere, *J. Geophys. Res.*, *77*(19), 3455–3474.
- Ma, Q., et al. (2015), Modeling inward diffusion and slow decay of energetic electrons in the Earth's outer radiation belt, *Geophys. Res. Lett.*, *42*, 987–995, doi:10.1002/2014GL062977.
- Ma, Q., et al. (2016), Simulation of energy-dependent electron diffusion processes in the Earth's outer radiation belt, *J. Geophys. Res. Space Physics*, *121*, 4217–4231, doi:10.1002/2016JA022507.
- MATLAB (2016), *Version 9.1 (R2016b)*, The MathWorks Inc., Natick, Mass.
- Meredith, N. P., R. B. Horne, R. H. Iles, R. M. Thorne, D. Heynderickx, and R. R. Anderson (2002), Outer zone relativistic electron acceleration associated with substorm-enhanced whistler mode chorus, *J. Geophys. Res.*, *107*(A7), 1144, doi:10.1029/2001JA900146.
- Meredith, N. P., R. B. Horne, S. A. Glauert, R. M. Thorne, D. Summers, J. M. Albert, and R. R. Anderson (2006), Energetic outer zone electron loss timescales during low geomagnetic activity, *J. Geophys. Res.*, *111*, A05212, doi:10.1029/2005JA011516.

- Meredith, N. P., R. B. Horne, S. A. Glauert, and R. R. Anderson (2007), Slot region electron loss timescales due to plasmaspheric hiss and lightning-generated whistlers, *J. Geophys. Res.*, *112*, A08214, doi:10.1029/2007JA012413.
- Milstein, G. N. (2002), The probability approach to numerical solution of nonlinear parabolic equations, *Numer. Meth. Partial Differ. Equ.*, *18*, 490–522, doi:10.1002/num.10020.
- Milstein, G. N., and M. V. Tretyakov (2001), Numerical solution of the Dirichlet problem for nonlinear parabolic equations by a probabilistic approach, *IMA J. Numer. Anal.*, *21*(4), 887–917, doi:10.1093/imanum/21.4.887.
- Milstein, G. N., and M. V. Tretyakov (2002), A probabilistic approach to the solution of the Neumann problem for nonlinear parabolic equations, *IMA J. Numer. Anal.*, *22*, 599–622, doi:10.1093/imanum/22.4.599.
- Ni, B., R. M. Thorne, Y. Y. Shprits, and J. Bortnik (2008), Resonant scattering of plasma sheet electrons by whistler-mode chorus: Contribution to diffuse auroral precipitation, *Geophys. Res. Lett.*, *35*, L11106, doi:10.1029/2008GL034032.
- Ni, B., R. M. Thorne, N. P. Meredith, R. B. Horne, and Y. Y. Shprits (2011), Resonant scattering of plasma sheet electrons leading to diffuse auroral precipitation: 2. Evaluation for whistler mode chorus waves, *J. Geophys. Res.*, *116*, A04219, doi:10.1029/2010JA016233.
- Ni, B., W. Li, R. M. Thorne, J. Bortnik, J. C. Green, C. A. Kletzing, W. S. Kurth, G. B. Hospodarsky, and M. de Soria-Santacruz Pich (2014), A novel technique to construct the global distribution of whistler mode chorus wave intensity using low-altitude POES electron data, *J. Geophys. Res. Space Physics*, *119*, 5685–5699, doi:10.1002/2014JA019935.
- Reeves, G. D., K. L. McAdams, R. H. W. Friedel, and T. P. O'Brien (2003), Acceleration and loss of relativistic electrons during geomagnetic storms, *Geophys. Res. Lett.*, *30*(10), 1529, doi:10.1029/2002GL016513.
- Reeves, G. D., et al. (2013), Electron acceleration in the heart of the Van Allen radiation belts, *Science*, *341*(6149), 991–994, doi:10.1126/science.1237743.
- Roederer, J. G. (1970), *Dynamics of Geomagnetically Trapped Radiation, Physics and Chemistry in Space*, vol. 2, Springer, New York.
- Schulz, M., and L. J. Lanzerotti (1974), *Particle Diffusion in the Radiation Belts, Physics and Chemistry in Space*, vol. 7, Springer, Berlin.
- Shprits, Y. Y., and B. Ni (2009), Dependence of the quasi-linear scattering rates on the wave normal distribution of chorus waves, *J. Geophys. Res.*, *114*, A11205, doi:10.1029/2009JA014223.
- Shprits, Y. Y., S. R. Elkington, N. P. Meredith, and D. A. Subbotin (2008a), Review of modeling of losses and sources of relativistic electrons in the outer radiation belt. I: Radial transport, *J. Atmos. Sol. Terr. Phys.*, *70*, 1679–1693, doi:10.1016/j.jastp.2008.06.008.
- Shprits, Y. Y., D. A. Subbotin, N. P. Meredith, and S. R. Elkington (2008b), Review of modeling of losses and sources of relativistic electrons in the outer radiation belt. II: Local acceleration and loss, *J. Atmos. Sol. Terr. Phys.*, *70*, 1694–1713, doi:10.1016/j.jastp.2008.06.014.
- Shprits, Y. Y., A. C. Kellerman, A. Y. Drozdov, H. E. Spence, G. D. Reeves, and D. N. Baker (2015), Combined convective and diffusive simulations: VERB-4D comparison with 17 March 2013 Van Allen Probes observations, *Geophys. Res. Lett.*, *42*, 9600–9608, doi:10.1002/2015GL065230.
- Strang, G. (1968), On the construction and comparison of difference schemes, *SIAM J. Numer. Anal.*, *5*(3), 506–517, doi:10.1137/0705041.
- Su, Z., F. Xiao, H. Zheng, and S. Wang (2010), STEERB: A three-dimensional code for storm-time evolution of electron radiation belt, *J. Geophys. Res.*, *115*, A09208, doi:10.1029/2009JA015210.
- Subbotin, D., and Y. Shprits (2009), Three-dimensional modeling of the radiation belts using the Versatile Electron Radiation Belt (VERB) code, *Space Weather*, *7*, S10001, doi:10.1029/2008SW000452.
- Subbotin, D., and Y. Shprits (2012), Three-dimensional radiation belt simulations in terms of adiabatic invariants using a single numerical grid, *J. Geophys. Res.*, *117*, A05205, doi:10.1029/2011JA017467.
- Summers, D., R. M. Thorne, and F. Xiao (1998), Relativistic theory of wave particle resonant diffusion with application to electron acceleration in the magnetosphere, *J. Geophys. Res.*, *103*, 20,487–20,500, doi:10.1029/98JA01740.
- Summers, D., B. Ni, N. P. Meredith, R. B. Horne, R. M. Thorne, M. B. Moldwin, and R. R. Anderson (2008), Electron scattering by whistler-mode ELF hiss in plasmaspheric plumes, *J. Geophys. Res.*, *113*, A04219, doi:10.1029/2007JA012678.
- Tao, X., A. A. Chan, J. M. Albert, and J. A. Miller (2008), Stochastic modeling of multidimensional diffusion in the radiation belts, *J. Geophys. Res.*, *113*, A07212, doi:10.1029/2007JA012985.
- Tao, X., J. M. Albert, and A. A. Chan (2009), Numerical modeling of multidimensional diffusion in the radiation belts using layer methods, *J. Geophys. Res.*, *114*, A02215, doi:10.1029/2008JA013826.
- Tao, X., L. Zhang, C. Wang, X. Li, J. M. Albert, and A. A. Chan (2016), An efficient and positivity-preserving layer method for modeling radiation belt diffusion processes, *J. Geophys. Res. Space Physics*, *121*, 305–320, doi:10.1002/2015JA022064.
- Thorne, R. M. (2010), Radiation belt dynamics: The importance of wave-particle interactions, *Geophys. Res. Lett.*, *37*, L22107, doi:10.1029/2010GL044990.
- Thorne, R. M., and C. F. Kennel (1971), Relativistic electron precipitation during magnetic storm main phase, *J. Geophys. Res.*, *76*(19), 4446–4453, doi:10.1029/JA076i019p04446.
- Thorne, R. M., B. Ni, X. Tao, L. Chen, W. Li, N. P. Meredith, R. B. Horne, and Y. Y. Shprits (2013), Correction to “Resonant scattering of plasma sheet electrons leading to diffuse auroral precipitation: 1. Evaluation for electrostatic electron cyclotron harmonic waves,” “Resonant scattering of plasma sheet electrons leading to diffuse auroral precipitation: 2. Evaluation for whistler mode chorus waves,” and “Evolution of pitch angle distributions following injection from the plasma sheet”, *J. Geophys. Res. Space Physics*, *118*, 839–842, doi:10.1002/jgra.50154.
- Tsyganenko, N., and M. Sitnov (2005), Modeling the dynamics of the inner magnetosphere during strong geomagnetic storms, *J. Geophys. Res.*, *110*, A03208, doi:10.1029/2004JA010798.
- Tu, W., X. Li, Y. Chen, G. D. Reeves, and M. Temerin (2009), Storm-dependent radiation belt electron dynamics, *J. Geophys. Res.*, *114*, A02217, doi:10.1029/2008JA013480.
- Tu, W., G. S. Cunningham, Y. Chen, M. G. Henderson, E. Camporeale, and G. D. Reeves (2013), Modeling radiation belt electron dynamics during GEM challenge intervals with the DREAM3D diffusion model, *J. Geophys. Res. Space Physics*, *118*, 6197–6211, doi:10.1002/jgra.50560.
- Turner, D. L., et al. (2014a), Competing source and loss mechanisms due to wave-particle interactions in Earth's outer radiation belt during the 30 September to 3 October 2012 geomagnetic storm, *J. Geophys. Res. Space Physics*, *119*, 1960–1979, doi:10.1002/2014JA019770.
- Turner, D. L., et al. (2014b), On the cause and extent of outer radiation belt losses during the 30 September 2012 dropout event, *J. Geophys. Res. Space Physics*, *119*, 1530–1540, doi:10.1002/2013JA019446.
- Ukhorskiy, A. Y., M. I. Sitnov, K. Takahashi, and B. J. Anderson (2009), Radial transport of radiation belt electrons due to stormtime Pc5 waves, *Ann. Geophys.*, *27*(5), 2173–2181, doi:10.5194/angeo-27-2173-2009.
- Van Allen, J. A., and L. A. Frank (1959), Radiation around the Earth to a radial distance of 107,400 km, *Nature*, *183*, 430–434, doi:10.1038/183430a0.
- Xiao, F., Z. Su, H. Zheng, and S. Wang (2010), Three-dimensional simulations of outer radiation belt electron dynamics including cross-diffusion terms, *J. Geophys. Res.*, *115*, A05216, doi:10.1029/2009JA014541.

- Xiao, F., et al. (2014), Chorus acceleration of radiation belt relativistic electrons during March 2013 geomagnetic storm, *J. Geophys. Res. Space Physics*, *119*, 3325–3332, doi:10.1002/2014JA019822.
- Zheng, L., A. A. Chan, J. M. Albert, S. R. Elkington, J. Koller, R. B. Horne, S. A. Glauert, and N. P. Meredith (2014), Three-dimensional stochastic modeling of radiation belts in adiabatic invariant coordinates, *J. Geophys. Res. Space Physics*, *119*, 7615–7635, doi:10.1002/2014JA020127.
- Zheng, L., A. A. Chan, T. P. O'Brien, W. Tu, G. S. Cunningham, J. M. Albert, and S. R. Elkington (2016), Effects of magnetic drift shell splitting on electron diffusion in the radiation belts, *J. Geophys. Res. Space Physics*, *121*, 11,985–12,000, doi:10.1002/2016JA023438.